The 11th International Congress
Motor Vehicles & Motors 2026
Kragujevac, Serbia
October 8th - 9th, 2026

Motor Vehicles & Motors

MVM2026-034
https://doi.org/10.24874/CMVM2026.034
Original scientific paper

Mihailo Đuković[1]
Saša Milojević[2]
Slobodan Savić[3]
Blaža Stojanović[4]
Horia Abaitancei[5]

APPLICATION OF A RADIAL HYDRAULIC MOTOR IN ALTERNATIVE VEHICLE DRIVE SYSTEMS

ABSTRACT: The transition toward alternative vehicle propulsion systems has created a need for innovative drive concepts capable of improving efficiency, reliability, and operational flexibility. This paper presents a concept of a vehicle drive system based on the application of a radial hydraulic motor. The proposed solution is analysed from the aspect of power transmission, torque generation, and potential integration into specialized vehicle platforms. Particular attention is given to the advantages of hydraulic drive systems in applications requiring high torque at low rotational speeds. The paper also discusses future research directions involving numerical simulations, performance verification, and possible implementation in lightweight transport vehicles and minibuses.

KEYWORDS: radial hydraulic motor, alternative propulsion systems, vehicle drive, hydraulic transmission, powertrain analysis

PRIMENA RADIJALNOG HIDROMOTORA U ALTERNATIVNIM POGONSKIM SISTEMIMA

REZIME: Prelazak na alternativne pogonske sisteme vozila stvorio je potrebu za inovativnim konceptima pogona koji mogu poboljšati efikasnost, pouzdanost i operativnu fleksibilnost. Ovaj rad predstavlja koncept sistema pogona vozila zasnovanog na primeni radijalnog hidrauličnog motora. Predloženo rešenje je analizirano sa aspekta prenosa

[1] *Mihailo Đuković, M.Sc. student, Faculty of Engineering University of Kragujevac, Kragujevac 34000, Sestre Janjić 6, Serbia, mihailo.djukovic.02@gmail.com*
[2] *Dr Saša Milojević, prof. assist. Faculty of Engineering University of Kragujevac, Kragujevac 34000, Sestre Janjić 6, Serbia, sasa.milojevic@kg.ac.rs, https://orcid.org/0000-0003-0569-047X*
[3] *Dr Slobodan Savić, full prof. Faculty of Engineering University of Kragujevac, Kragujevac 34000, Sestre Janjić 6, Serbia, ssavic@kg.ac.rs, https://orcid.org/0000-0001-6609-4845*
[4] *Dr Blaža Stojanović, full prof. Faculty of Engineering University of Kragujevac, Kragujevac 34000, Sestre Janjić 6, Serbia, blaza@kg.ac.rs, https://orcid.org/0000-0003-4790-2856*
[5] *Dr Horia Abaitancei, full prof. Institute of Automotive Engineering Transilvania University of Brasov, Brasov, Strada Insitutului 9, Romania, h.abaitancei@unitbv.ro, https://orcid.org/0009-0001-8569-2194*

snage, generisanja obrtnog momenta i potencijalne integracije u specijalizovane platforme vozila. Posebna pažnja je posvećena prednostima hidrauličnih pogonskih sistema u primenama koje zahtevaju visok obrtni moment pri malim brzinama rotacije. U radu se takođe razmatraju budući pravci istraživanja koji uključuju numeričke simulacije, verifikaciju performansi i moguću implementaciju u lakim transportnim vozilima i minibusevima.

KLJUČNE REČI: radijalni hidraulični motor, alternativni pogonski sistemi, pogon vozila, hidraulični prenos, analiza pogonskog sklopa

INTRODUCTION

Modern transport vehicles require high efficiency, reliability, and operational flexibility under increasingly demanding urban and interurban operating conditions. Frequent acceleration and deceleration, variable payloads, and the requirement for compact and efficient drivetrain configurations necessitate the development of alternative propulsion architectures. Consequently, the development of high-performance and flexible vehicle drive systems remains an important research direction in modern transportation engineering (Guzzella & Sciarretta, 2005).

Conventional mechanical transmissions offer high efficiency but suffer from structural complexity, substantial weight, and limited flexibility in torque distribution and drivetrain layout. These limitations drive the investigation of alternative vehicle propulsion concepts. In modern vehicle design, individual in-wheel electric drives have attracted significant attention due to their ability to provide independent torque control at individual wheels, improving traction control and vehicle manoeuvrability (Popovici et al. 2026). However, the application of electric hub drives may involve challenges related to power density, thermal management, and integration of electric components within the wheel assembly, particularly in vehicles with increased mass and demanding operating conditions. In this context, hydrostatic radial piston drives represent a promising alternative for transport vehicles and minibuses requiring high starting torque and compact drivetrain configurations (Tanaka et al. 2013).

Hydrostatic systems can transmit substantial power within compact dimensions, providing flexibility in drivetrain packaging and the arrangement of the prime mover and wheel-drive units. Comparative evaluations of electric, hydraulic, and pneumatic rotary actuation systems indicate that hydraulic solutions can provide high torque density and favourable low-speed operating characteristics, making them suitable for vehicle propulsion applications (Tanaka et al. 2013). Among hydraulic solutions, multi-stroke radial piston motors are particularly promising due to their High-Torque Low-Speed (HTLS) characteristics, making them well suited for direct or near-direct wheel-drive applications requiring high starting torque, compact installation, and flexible power transmission (Abaitancei et al. 2016; Li et al. 2024; Mannesmann, 1998; Dindorf, 2024; Bašta, 1986; Savić, 1986)

The objective of this paper is to investigate the application of radial piston hydraulic motors in transport vehicle and minibus drivetrains using a multi-domain simulation model developed in *Simcenter Amesim* (Siemens Digital Industries Software, 2020). The proposed drive concept is analysed from the aspects of power transmission, torque generation, volumetric leakage, and thermal behaviour under representative vehicle operating conditions. The scientific contribution of this work lies in the development and application of a mathematical and simulation framework for evaluating the suitability of radial hydraulic motors as an alternative propulsion solution for transport vehicles and minibuses, providing a basis for further optimization, performance verification, and experimental validation.

HYDRAULIC PROPULSION SYSTEMS

Hydrostatic drive systems represent an important alternative to conventional mechanical transmissions in modern motor vehicles, particularly in applications requiring continuous speed regulation and high torque at low rotational speeds. In a hydrostatic drive, mechanical energy supplied by the prime mover is converted into hydraulic energy by a hydraulic pump and subsequently converted back into mechanical energy by one or more hydraulic motors (Abaitancei et al. 2016; Krstić, 2003).

The application of hydrostatic drive systems (HST) in mobile machines and specialized vehicles is motivated by the need for flexible drivetrain configurations, compact component arrangement, and precise control of vehicle speed and wheel torque. Unlike conventional mechanical transmissions, hydrostatic drives enable stepless speed regulation and rapid changes in the direction of rotation without the need for conventional multi-stage gearboxes. These characteristics make hydrostatic systems particularly suitable for vehicles operating under variable load conditions and requiring high starting torque and precise low-speed control (Abaitancei et al. 2016; Krstić, 2003).

The hydrostatic drivetrain considered in this work is based on the use of a hydraulic pump connected to the prime mover and radial piston hydraulic motors integrated into the drive-wheel assemblies. This configuration eliminates several conventional mechanical transmission components, such as the mechanical gearbox, cardan shafts, and conventional differentials, allowing greater flexibility in drivetrain packaging and torque distribution (Abaitancei et al.

2016; Savić, 1986; Krstić, 2003). The proposed system architecture and the corresponding hydraulic fluid flow paths are presented in Figure 1.

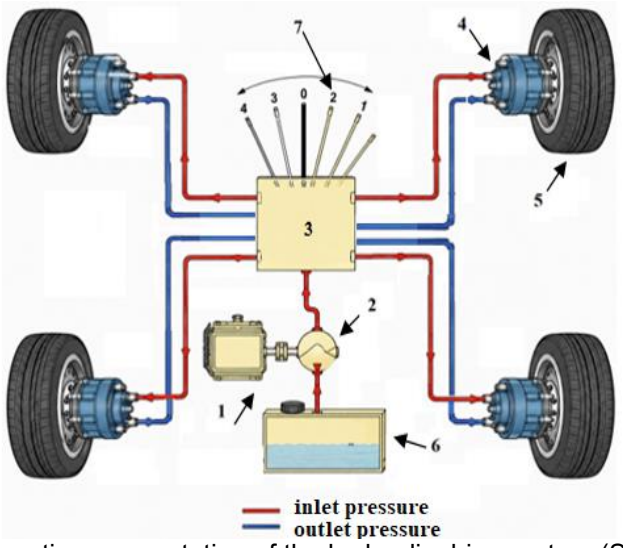


Figure 1 Schematic representation of the hydraulic drive system (Sonale, 2024)

In vehicles equipped with a hydrostatic drivetrain, the main components include the prime mover, hydraulic pump, hydraulic motors, directional and control valves, reservoir, and fluid lines. The system operates by circulating hydraulic fluid through a closed hydraulic circuit. The prime mover (1), which may be an internal combustion engine, electric motor, or another mechanical energy source, drives the hydraulic pump (2). The pump draws hydraulic fluid, typically oil, from the reservoir (6) and supplies it to the hydraulic circuit (Abaitancei et al. 2016; Savić, 1986; Krstić, 2003).

The load generated by the hydraulic motors and flow resistance establishes the required fluid pressure in the delivery line. Pressurized fluid (red lines) is directed through the control valve block (3), which regulates its flow toward the hydraulic motors integrated into the wheel hubs (4). This configuration enables the hydraulic energy to be independently supplied to individual drive wheels, providing increased flexibility in drivetrain layout and torque distribution (Abaitancei et al. 2016; Savić, 1986; Krstić, 2003).

The radial piston hydraulic motors convert the hydraulic energy into mechanical power. Fluid pressure acts on the motor pistons, producing reciprocating motion that is transformed into rotary motion of the rotor and drive wheel (5). The generated torque provides the driving force required for vehicle propulsion. After passing through the motor, the low-pressure fluid (blue lines) returns to the reservoir (6), where it can be cooled and filtered before re-entering the hydraulic circuit, depending on the system configuration (Savić, 1986; Krstić, 2003).

RADIAL HYDRAULIC MOTOR

The radial piston hydraulic motor is a low-speed, high-torque hydraulic motor widely used in applications requiring high torque at relatively low rotational speeds (Figure 2). Its operating principle is based on the conversion of hydraulic energy into mechanical energy through the radial reciprocating motion of pistons. Due to their high torque density, compact configuration, and ability to operate at low speeds, radial piston motors are suitable for applications requiring high starting torque and precise low-speed operation (Bašta, 1986; Savić, 1986).

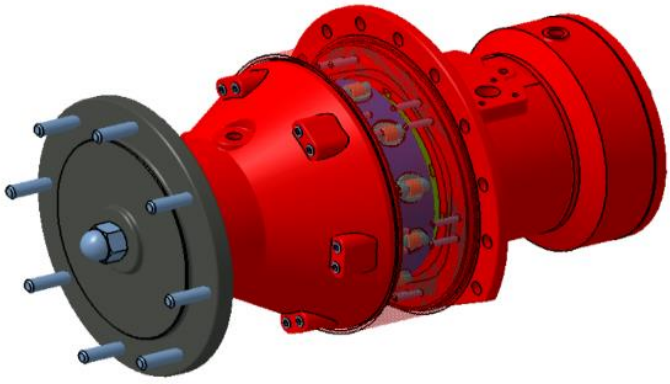


Figure 2 3D model of Radial piston hydraulic motor

The multi-stroke radial piston hydraulic motor features a robust construction designed to withstand high hydraulic pressures and demanding operating conditions. Its specific geometry and kinematic configuration enable multiple working strokes during a single rotor revolution, resulting in high displacement and torque generation at relatively low rotational speeds. These characteristics make radial piston motors particularly suitable for direct or near-direct wheel-drive applications in transport vehicles and minibuses (Bašta, 1986; Savić, 1986; Giavarini 2022).

Construction and principle

A multi-stroke radial piston hydraulic motor consists of several main components, as illustrated in Figure 3:

1. Cam-profile stator: the stationary component with a multi-lobe internal cam profile that determines the piston displacement and number of working strokes per rotor revolution.
2. Rotor (cylinder block): the rotating component containing the radially arranged cylinder chambers. It is connected to the output shaft and transfers the generated torque to the driven element.
3. Piston assemblies with rollers: radially arranged pistons that reciprocate within the cylinder chambers. Rollers at the outer ends of the pistons maintain contact with the stator profile and transmit the generated force to the rotor.
4. Flow distribution pair: the hydraulic distribution mechanism that controls the connection between the individual cylinder chambers and the high- and low-pressure ports, ensuring the appropriate sequence of fluid admission and discharge.
5. Output drive shaft: the rotating shaft through which the generated torque is transmitted to the driven wheel or other mechanical load.
6. Motor housing (casing): the stationary outer housing that supports the internal components and provides structural protection for the motor assembly.

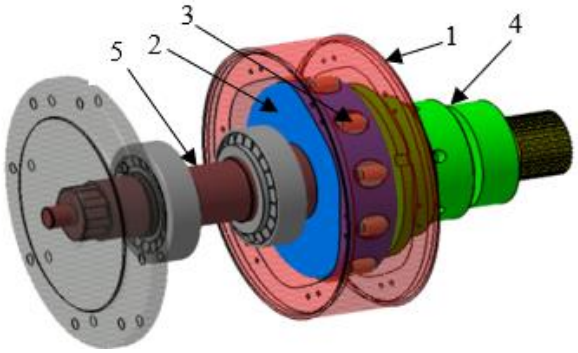


Figure 3 Key parts of radial hydraulic motor

The operating principle is based on the conversion of hydraulic energy into mechanical torque through cyclic radial piston motion. During the working stroke, pressurized hydraulic fluid is supplied to a cylinder chamber through the flow distribution pair (4). The resulting pressure force moves the piston (3) radially outward. The piston roller follows the cam profile of the stator (1), generating a tangential force that produces rotation of the rotor (2) and output shaft (5) (Giavarini 2022).

As the rotor continues to rotate, the piston reaches the end of its working stroke and the corresponding cylinder chamber is disconnected from the high-pressure supply. During the return stroke, the geometry of the stator profile causes the piston to move radially inward while the flow distribution pair connects the chamber to the low-pressure outlet. The hydraulic fluid is consequently discharged from the chamber (Giavarini 2022).

The continuous repetition of these cycles produces rotary motion of the output shaft and enables the motor to generate high torque at low rotational speeds. The resulting torque characteristics make radial piston motors suitable for applications in which high starting torque and controlled low-speed operation are required, such as transport vehicles operating under frequent acceleration and deceleration (Giavarini 2022).

The internal clearances between the piston-cylinder interfaces and within the flow distribution pair are important for the volumetric performance of the motor. Under elevated pressure differences, these clearances can result in internal volumetric leakage, reducing the effective flow available for torque generation and consequently affecting the overall efficiency of the motor. Therefore, the analysis and quantification of internal leakage represent an important aspect of evaluating radial piston motors for vehicle propulsion applications (Giavarini 2022).

Main characteristics and comparison with conventional drivetrains

Radial piston hydraulic motors are classified as high-torque, low-speed (HTLS) displacement machines. Their multi-stroke operating principle enables several working strokes during one rotor revolution, resulting in high displacement and torque generation at relatively low rotational speeds (Tanaka et al., 2013). This characteristic is particularly advantageous for wheel-drive applications, where high starting torque and controlled low-speed operation are required.

When integrated into a hydrostatic drivetrain, radial piston motors can be positioned directly at or near the driven wheels. Such an architecture can reduce the number of conventional mechanical transmission components, including mechanical gearboxes, drive shafts, and differentials, depending on the selected drivetrain configuration. This provides greater flexibility in component arrangement and may contribute to more compact drivetrain packaging and simplified torque distribution (Bašta, 1986; Savić, 1986; Giavarini 2022).

Compared with axial piston hydraulic motors, radial piston motors generally provide lower rotational speeds and higher torque characteristics, making them particularly suitable for direct-drive applications. Axial piston motors used for wheel propulsion may require additional mechanical reduction depending on the required wheel torque and operating speed. The use of a radial piston motor can therefore reduce or eliminate the need for additional mechanical reduction in applications where its speed and torque characteristics match the requirements of the driven wheel (Bašta, 1986; Savić, 1986; Giavarini 2022).

For transport vehicles and minibuses, these characteristics can be particularly relevant during vehicle launch, low-speed manoeuvring, and frequent stop-and-go operation. The combination of high starting torque, compact installation, and flexible hydraulic power distribution makes radial piston motors a potential alternative to conventional mechanical drivetrain configurations.

APPLICATION OF RADIAL HYDRAULIC MOTORS TO EASY TRANSPORT VEHICLES AND MINIBUSES

Radial piston hydraulic motors have a specific and practical application on easy transport vehicles like mini – trucks and minibuses. They are used in these vehicles primarily due to the need for compactness, high starting torque and the elimination of heavy mechanical components. Urban transport solutions and light-duty commercial vehicles operate under distinct spatial constraints and highly transient duty cycles (Figure 4). To optimize chassis packaging and maximize structural volume, a decentralized hydrostatic propulsion framework is introduced. This layout bypasses the rigid configurations imposed by conventional multi-speed gearboxes, split differentials, and linear drive shafts, offering an inherently modular fluid-power alternative (Abaitancei et al., 2016; Dindorf, 2024).

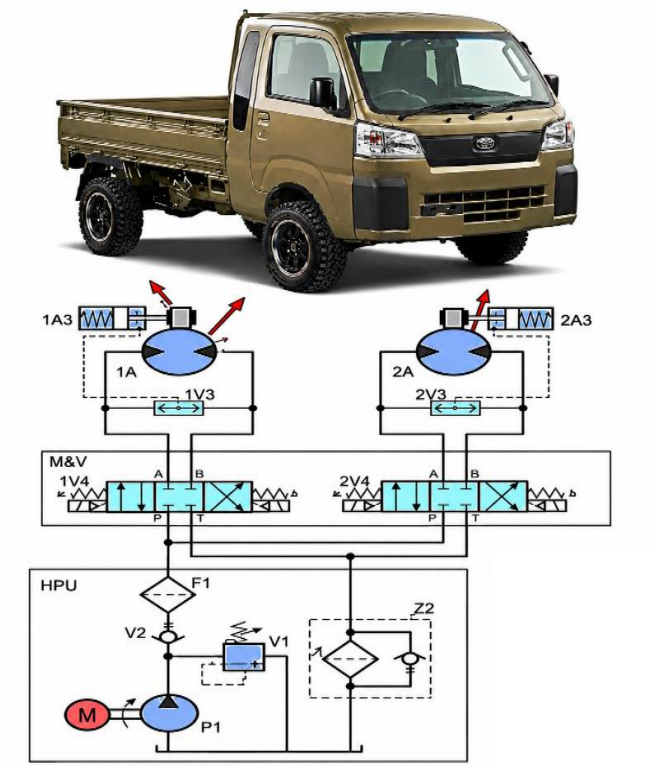


Figure 4 Schematic diagram of conventional hydraulic propulsion system of the mini – truck

The structural deployment of the system relies on an integrated fluid delivery network segregated into three operational segments: the Central Generating Group, the Symmetric Flow Distribution Nodes, and the Peripheral Hub Actuating Units. Mechanical power from the prime mover—which can be tailored as a highly efficient internal combustion engine or a zero-emission electric motor—is directly converted into hydraulic energy via a variable displacement axial piston pump (P1) equipped with electro-proportional displacement control (Dindorf, 2024).

To safeguard the closed-loop system against transient pressure spikes during abrupt decelerations, a dual-directional flushing and shock-absorber valve manifold is integrated directly at the pump boundary (Abaitancei et al. 2016; Mannesmann, 1998; Dindorf, 2024). System fluid undergoes continuous purification through a micro-glass media filter situated in the low-pressure charging line, while operating temperatures are strictly regulated by a modulated, smart-bypass air-oil cooling matrix to ensure stable fluid viscosity during intense stop-and-go driving profiles.

Power allocation to the traction points is governed by two decentralized Axial Manifold Blocks (AMB-L and AMB-R), which act as an intelligent fluid-power differential. The left-side manifold distributes high-pressure oil in a parallel loop to the front and rear radial-piston hub motors (M-1 and M-2), while the right-side manifold simultaneously supplies motors M-3 and M-4 (Mannesmann, 1998; Dindorf, 2024).

This fluid-power configuration introduces distinct operational paradigms specifically engineered for light utility platforms and passenger minibuses (Mannesmann, 1998; Dindorf, 2024):

- Volumetric Floor Optimization in Passenger Transports: Traditional mechanical drivetrains dictate the chassis height due to the physical envelope of the transmission tunnel and rear axle differential housings. By integrating multi-cam radial piston motors directly within the wheel rims, all mechanical driveline components are completely extracted from the under-chassis zone. This facilitates an absolute low-floor configuration, creating a continuous, flat passenger platform that optimizes cabin ergonomics, increases standing passenger capacity, and ensures rapid, step-free ingress and egress.
- Dynamic Work-Cycle Adaptability for Light Utility Vehicles: Light commercial mini-trucks require extreme torque variability when transitioning from empty highway transit to fully laden, low-speed work operations (e.g., municipal maintenance or waste collection). The multi-stroke radial motors utilized in this system feature selectable displacement configurations (multi-displacement switching). At low speeds, the motors operate at full volumetric displacement to maximize starting tractive effort and gradeability. For high-speed transport, individual motor sub-chambers can be hydraulically isolated or shifted into a low-drag freewheeling state, drastically minimizing parasitic fluid shear losses and boosting fuel economy.

Mathematical model

To evaluate the conceptual performance of a high-torque radial piston hydraulic motor for light-duty transit and utility operations, a comprehensive mathematical model is established. This model defines the relationship between hydraulic input energy, internal mechanical and volumetric losses, and the dynamic output performance required to propel mini-trucks and minibuses under demanding urban stop-and-go profiles and variable payload conditions.

The rotational speed of the radial hydraulic motor is directly governed by the volumetric flow rate of the hydraulic fluid supplied to its cylinders. The theoretical flow rate Q_{th} [m³ s⁻¹], which assumes zero leakage and ideal geometry, is defined as (Giavarini 2022):

$$Q_{th} = V_d \cdot n \tag{1}$$

where:

- V_d is the displacement of the radial motor [m³ rev^{-1}];
- n is the rotational speed of the motor shaft [rps].

In light commercial vehicles and minibuses, high operational pressures during acceleration from a standstill lead to internal fluid bypass across the piston-cylinder clearances and the distribution valves. Therefore, the actual flow rate Q_{act} required by the motor is expressed as (Giavarini 2022):

$$Q_{act} = Q_{th} + Q_{leak} \tag{2}$$

where Q_{leak} represents the internal volumetric leakage flow rate [m³ s^{-1}].

Radial piston motors are categorized as Low-Speed High-Torque (LSHT) drives, making them ideal for mini-trucks handling maximum payload launch efforts and transit platforms navigating steep urban inclines. The ideal or theoretical torque T_{th} [Nm] generated by the motor depends strictly on its geometric displacement and the differential pressure (Giavarini 2022):

$$T_{th} = \frac{V_d \, \Delta p}{2\pi} \tag{3}$$

where

$$\Delta p = p_{in} - p_{out} \tag{4}$$

is the pressure drop across the motor [Pa].

The actual torque T_{act} delivered to the vehicle's wheel hub is lower than the theoretical value due to mechanical friction between moving components (pistons, rollers, and multi-cam lobes). It is calculated as (Giavarini 2022):

$$T_{act} = T_{th} - T_{loss} = T_{th}\eta_{hm} \tag{5}$$

where:

- T_{loss} is the total friction torque loss [Nm];
- η_{hm} is the hydro-mechanical efficiency of the motor.

The conversion of hydraulic power into mechanical power determines the overall tractive and acceleration capability of the commercial vehicle. The hydraulic input power P_{hyd} [W] delivered by the system pump is given by (Giavarini 2022):

$$P_{hyd} = Q_{act} \, \Delta p \tag{6}$$

The effective mechanical power P_{mech} [W] available at the output wheel hub to drive the mini-truck or minibus is defined as (Giavarini 2022):

$$P_{mech} = T_{act}\omega = T_{act} \frac{2\pi n_{rpm}}{60} \tag{7}$$

where:

- ω is the angular velocity of the shaft [rad/s];
- n_{rpm} is the shaft speed in revolutions per minute [rpm].

Compact utility platforms and minibuses operate under highly variable thermal cycles due to intensive braking energy recovery and continuous urban idling, which drastically alters oil viscosity and loss characteristics. The internal leakage flow Q_{leak} can be mathematically modeled using the Wilson-based hydraulic loss approach (Giavarini 2022):

$$Q_{leak} = \frac{C_s V_d \Delta p}{\mu} \tag{8}$$

where:

- C_s is the dimensionless laminar leakage coefficient of the radial motor;
- μ is the dynamic viscosity of the hydraulic fluid [Pa·s].

The volumetric efficiency η_v is then formulated as (Giavarini 2022):

$$\eta_v = \frac{Q_{th}}{Q_{act}} = 1 - \frac{Q_{leak}}{Q_{act}} \tag{9}$$

The torque loss T_{loss} comprises both Coulomb (constant) friction and viscous fluid shear friction within the motor housing (Giavarini 2022):

$$T_{loss} = \left(C_f V_d \Delta p\right) + \left(C_v V_d \mu \omega\right) \tag{10}$$

where:

- C_f is the mechanical friction coefficient;
- C_v is the viscous drag coefficient.

Consequently, the total efficiency of the hydraulic drive η_t is expressed as (Giavarini 2022):

$$\eta_t = \eta_v \eta_{hm} = \frac{P_{mech}}{P_{hyd}} \tag{10}$$

After defining the geometric relationships and theoretical flow characteristics within the radial piston hydraulic motor itself, it is necessary to establish a connection between the internal operating parameters of the fluid and the external resistances acting on the vehicles. Since the analyzed hydraulic motor is intended for direct wheel drive, the operating pressure and required fluid power are directly dictated by the road requirements in terms of torque and power. For this reason, a dynamic analysis of the vehicles was carried out below by identifying individual types of friction and resistance to movement that occur in real operating conditions.

Rolling resistance primarily depends on the hysteresis of the tire material, friction due to microslip at the tire-road contact, and friction within the wheel bearing assembly itself. Since the rolling resistance coefficient is affected by a large number of factors (vehicle speed, tire pressure, load, soil characteristics), the following polynomial formulations for force F_{roll}, torque T_{roll}, and power P_{roll} are used to evaluate this resistance at a generic road gradient (Giavarini 2022; Wong, 2008):

$$F_{roll} = m \cdot g \cdot k \cdot \cos\alpha \tag{11}$$

$$T_{roll} = m \cdot g \cdot r_w \cdot k \cdot \cos\alpha \tag{12}$$

$$P_{roll} = m \cdot g \cdot k \cdot v \cdot \cos\alpha \tag{13}$$

where:

- m is total vehicle mass [kg],
- g is acceleration due to gravity [m s^{-2}],
- r_w is wheel radius [m],
- v is truck speed [m/s] and
- α – road gradient [°].

Aerodynamic drag depends on the air density ρ, the vehicle frontal area A_f, the drag coefficient C_f, and the relative speed of the vehicle v_r. Its classical formulation for force, moment, and power is defined by the expressions (Giavarini 2022; Wong, 2008):

$$F_a = \frac{1}{2} \cdot \rho \cdot A_f \cdot C_f \cdot {v_r}^2 \tag{14}$$

$$T_a = \frac{1}{2} \cdot \rho \cdot A_f \cdot C_f \cdot {v_r}^2 \cdot r_w \tag{15}$$

$$P_a = \frac{1}{2} \cdot \rho \cdot A_f \cdot C_f \cdot {v_r}^3 \tag{16}$$

The vehicle frontal area A_f in equations (14—16) represents the projected front surface of the chassis and is determined based on the overall vehicle dimensions using the empirical formulation (Wong, 2008):

$$A_f = W \cdot H \cdot k \tag{20}$$

where:

- W is the overall vehicle width (excluding mirrors) [m],
- H is the overall vehicle height [m], and
- k is the empirical shape factor, which ranges between 0.80 and 0.85 for the considered vehicle classes (commercial vans and light trucks with rounded profiles) [16].

These values are completely independent of the road gradient. When driving on a flat road $\alpha = 0$, the characteristic speed v_c represents the point at which rolling resistance and aerodynamic drag are equal. Due to the speed-level dependence, for all values $v < v_c$ rolling resistance dominates, while at higher speeds aerodynamic drag becomes the dominant factor (Giavarini 2022).

The component of the drag force that directly depends on the angle of inclination of the surface α and the weight of the vehicle is determined through the following system of equations (Giavarini 2022; Wong, 2008):

$$F_s = m \cdot g \cdot \sin\alpha \tag{17}$$

$$T_s = m \cdot g \cdot r_w \cdot \sin\alpha \tag{18}$$

$$P_s = m \cdot g \cdot v \cdot \sin\alpha \tag{19}$$

When achieving acceleration a, the inertial load of the rotating parts must be properly taken into account via the apparent mass of the vehicle m_{app} (Giavarini 2022; Wong, 2008):

$$m_{app} = m + J_{mot} \cdot \frac{{\tau_I}^2}{{r_w}^2} + J_{trans} \cdot \frac{{\tau_{II}}^2}{{r_w}^2} + \frac{J_w}{{r_w}^2} \tag{20}$$

Where J_x represents the moments of inertia of individual rotating elements (engine, transmission and wheels), while τ_I and τ_{II} are the gear ratios between individual subassemblies (in the case of direct in-wheel drive where the hydraulic motor is inside the hub, these gear ratios are 1). The impact of acceleration on the dynamic demands of the vehicle is expressed as (Giavarini 2022; Wong, 2008):

$$F_{app} = m_{app} \cdot a \tag{21}$$

$$M_{app} = m_{app} \cdot a \cdot r_w \tag{22}$$

$$P_{app} = m_{app} \cdot a \cdot v \tag{23}$$

By knowing all the individual resistance components, it is possible to precisely quantify at any time the total required torque and power that the radial piston hydraulic motors must deliver to the vehicle wheels for any defined road driving conditions.

SIMULATION MODEL, RESULTS AND DISCUSSION

To evaluate the hydrostatic powertrain concept for light commercial configurations and tactical transport applications, a comprehensive multi-domain simulation model was established within the *Simcenter Amesim* environment (Siemens Digital Industries Software, 2020). The developed simulation frameworks directly couple the high-pressure hydraulic network with the longitudinal dynamics of two-axle vehicle platforms, with the powertrain topologies structurally differentiated according to the technical designs and specific operational requirements of each vehicle class. Figure 5 illustrates the multi-domain simulation scheme for the lightweight transport vehicle platform.

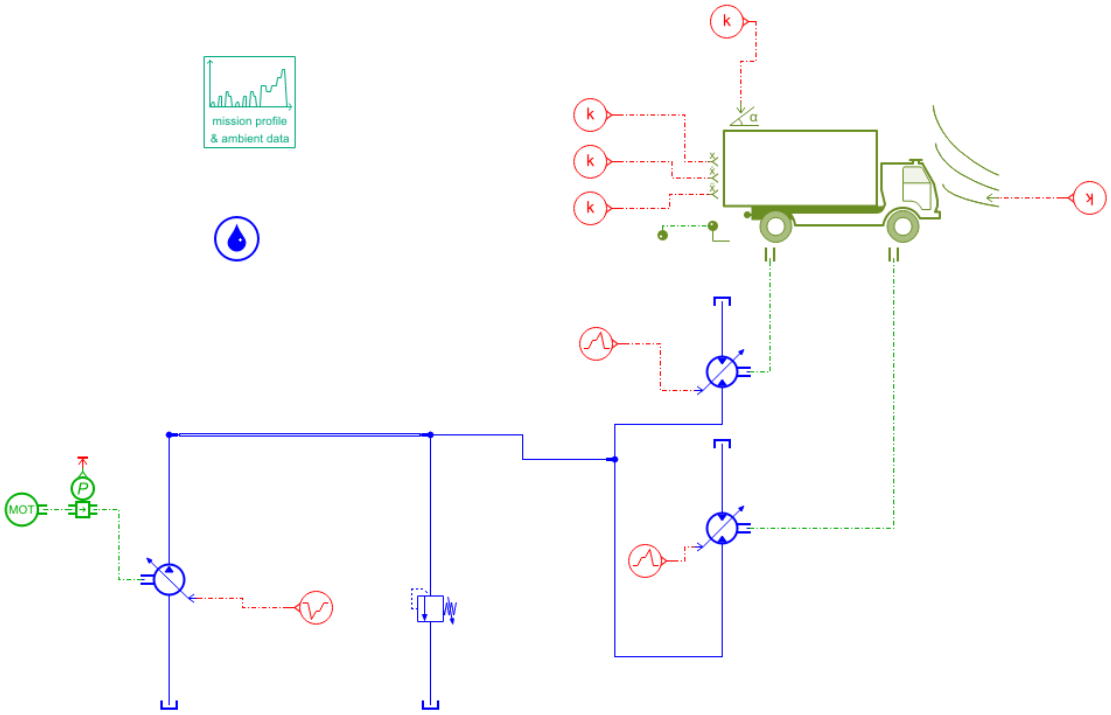


Figure 5 The lightweight transport vehicle drive diagram (Siemens Digital Industries Software, 2020)

The hydrostatic drive layer of both models consists of a primary pump unit that delivers the working fluid under pressure to the radial piston hydraulic motors located in the vehicle wheels. An advanced feature of this multi-domain concept is reflected in the integration of dynamic boundary conditions of the external environment (via a block diagram with k-coefficients), which actively introduces the effects of terrain slope, aerodynamic drag, and variable tire rolling resistance into the calculation. In order to provide a comprehensive analysis and verification under different

operating conditions, simulations were conducted independently. The basic geometric, aerodynamic, and hydraulic parameters implemented in these simulation frameworks are summarized in Table 1 (for the Suzuki Carry DA16T mini-truck) and Table 2 (for the Toyota HiAce V minibus).

Table 1 Operational parameters of the Suzuki Carry DA16T (Carfolio, n.d.; Wong, 2008; Totten & De Negri, 2012)

Quantity	Values	Reference
Total vehicle mass	1100 kg	Vehicle specification (Carfolio, n.d.)
Tire Specification	145/80 - R12 (r = 0.268 m)	Vehicle specification (Carfolio, n.d.)
Prime Mover Speed	2000 rpm	Simulation boundary condition (Siemens Digital Industries Software, 2020)
Engine power	37 [kW]	Standard engine parameter (Carfolio, n.d.)
Pump Displacement	200 [$cm^3\,rev^{-1}$]	Simulation boundary condition (Siemens Digital Industries Software, 2020)
In-Wheel Motors Displacement	125 [$cm^3\,rev^{-1}$]	Simulation boundary condition (Siemens Digital Industries Software, 2020)
Vehicle length	3395 [mm]	Standard vehicle dimensions (Carfolio, n.d.)
Vehicle width	1475 [mm]	Standard vehicle dimensions (Carfolio, n.d.)
Vehicle height	1765 [mm]	Standard vehicle dimensions (Carfolio, n.d.)
Rolling resistance coeficient	0.015	Road condition parameter (Wong, 2008)
Aerodynamic drag coeficient	0.45	Aerodynamic property for this vehicle type (Carfolio, n.d.)
Vehicle frontal area	2 [m^2]	Determined via vehicle geometry (Carfolio, n.d.)
Fluid density	850 [$kg\,m^{-3}$]	Hydraulic oil property (Totten & De Negri, 2012)
Dynamic viscosity	51 cP	Hydraulic oil property (Totten & De Negri, 2012)
Road slope	0 %	Flat terrain baseline
Wind velocity	10 [$m\,s^{-1}$]	Headwind condition

Table 2 Operational parameters of the Toyota HiAce V (Auto-Data, n.d.; Wong, 2008; Totten & De Negri, 2012)

Quantity	Values	Reference
Total vehicle mass	3100 kg	Vehicle specification (Auto-Data, n.d.)
Tire Specification	185/75 R15 (r = 0.329 m)	Vehicle specification (Auto-Data, n.d.)
Prime Mover Speed	2000 rpm	Simulation boundary condition (Siemens Digital Industries Software, 2020)
Engine power	100 kW	Standard engine parameter (Auto-Data, n.d.)
Pump Displacement	500 [$cm^3\,rev^{-1}$]	Simulation boundary condition (Siemens Digital Industries Software, 2020)
In-Wheel Motors Displacement	250 [$cm^3\,rev^{-1}$]	Simulation boundary condition (Siemens Digital Industries Software, 2020)
Vehicle length	4695 [mm]	Standard vehicle dimensions (Auto-Data, n.d.)
Vehicle width	1695 [mm]	Standard vehicle dimensions (Auto-Data, n.d.)
Vehicle height	1980 [mm]	Standard vehicle dimensions (Auto-Data, n.d.)
Rolling resistance	0.015	Road condition parameter (Wong, 2008)
Aerodynamic drag coeficient	0.38	Aerodynamic property for this vehicle type (Auto-Data, n.d.)
Vehicle frontal area	2.8 [m^2]	Determined via vehicle geometry (Auto-Data, n.d.)
Fluid density	850 [$kg\,m^{-3}$]	Hydraulic oil property (Totten & De Negri, 2012)
Dynamic viscosity	51 cP	Hydraulic oil property (Totten & De Negri, 2012)
Road slope	0 %	Flat terrain baseline
Wind velocity	10 [$m\,s^{-1}$]	Headwind condition

The headwind velocity of 10 m/s (World Meteorological Organization [WMO], 2021) was adopted as a representative boundary condition for moderate gale testing environment to evaluate the powertrain under demanding ambient

factors. The aerodynamic drag coefficients C_f of 0.45 for the mini-truck and 0.38 for the minibus are selected based on standard empirical vehicle data from the literature for open-bed utility platforms and standard single-volume van profiles, respectively. The dynamic speed response of a light commercial vehicle and a minibus operating under a headwind profile of 10 [m s-1] are shown in Figures 6 and 7.

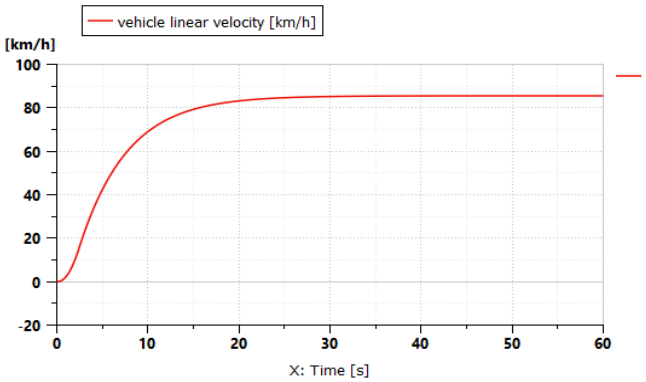


Figure 6 Diagram of simulated mini – truck velocity in 60 s operational cycle (Siemens Digital Industries Software, 2020)

The mini-truck's transient response comprises three distinct operating phases. During the initial activation (0–2 s), the vehicle remains stationary while the prime mover accelerates to 2000 rpm and pilot pressure disengages the spring-applied hydraulically released (SAHR) hub brakes. Once fully released, progressive acceleration begins. The high geometric displacement of the in-wheel radial piston motors generates substantial starting torque, enabling the 1100 kg chassis to overcome static inertia. Due to realistic power and torque limits now imposed on the prime mover, the acceleration curve exhibits a physical, non-linear trend as rolling and aerodynamic resistances scale with speed. Beyond the 25th second of the 60-second cycle, the vehicle reaches a quasi-steady state, asymptotically stabilizing at a maximum cruising velocity of approximately 85 km/h. This updated response validates the drivetrain's capability to deliver realistic transit performance under continuous aerodynamic loading.

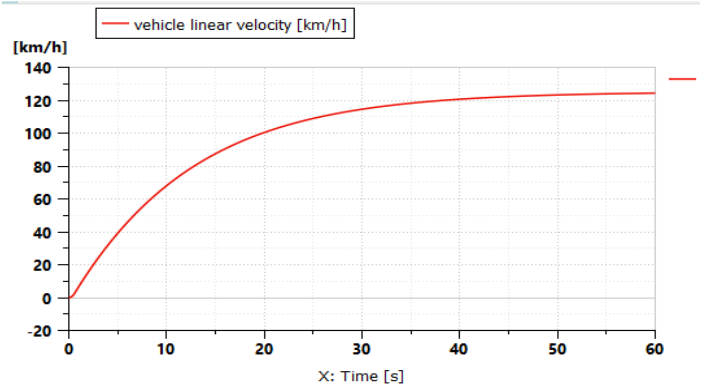


Figure 7 Diagram of simulated minibus velocity in 60s operational cycle (Siemens Digital Industries Software, 2020)

The larger minibus platform exhibits a distinct dynamic behavior due to its significantly higher mass of 3500 kg. While the initial pressure buildup and SAHR brake disengagement require roughly 1.5 seconds, the subsequent acceleration phase demands a greater energy throughput to counteract the increased structural inertia. To sustain velocity buildup under these conditions, the layout utilizes an optimized pump displacement of 500 cm^3/rev feeding the dual 250 cm^3/rev in-wheel motors. The resulting acceleration curve shows a more gradual gradient than the light truck, reflecting the physical impact of realistic prime mover torque limits. As velocity increases, aerodynamic drag—amplified by the larger 2.82 m^2 frontal area—becomes the dominant resistance factor, causing the acceleration to taper off asymptotically. The minibus eventually establishes a steady-state cruise beyond the 55th second, leveling off at 125 km/h. This response validates that the scaled hydrostatic configuration provides sufficient power reserves without violating physical boundaries.

The dynamic torque requirements at the wheel hubs of these vehicles are quantified in Figures 8 and 9.

The transient wheel torque response directly mirrors the vehicle's velocity profile phases. Since the total driving torque is equally distributed among the traction points, the diagram illustrates the localized torque input at a single axle (Port 2). During the initial launch phase (0–2.5 s), the axle torque rapidly escalates to a peak of approximately 580 Nm. This maximum effort is critical to overcome static chassis inertia and counteract the dynamic resistance during SAHR hub brake disengagement. Immediately following this peak, as the vehicle gains velocity, the torque

profile exhibits a smooth exponential decay, marking the transition to steady-state cruising. By the 25th second of the expanded 60-second cycle, the torque stabilizes at a quasi-steady value of approximately 105 Nm. This residual torque represents the continuous mechanical effort required by each in-wheel radial motor to actively balance the combined aerodynamic drag and rolling resistance at maximum cruising speed.

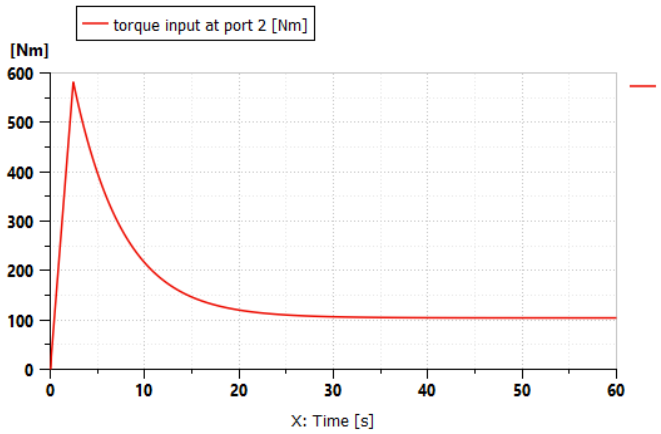


Figure 8 Simulated torque input profile at one axle of the mini – truck (Siemens Digital Industries Software, 2020)

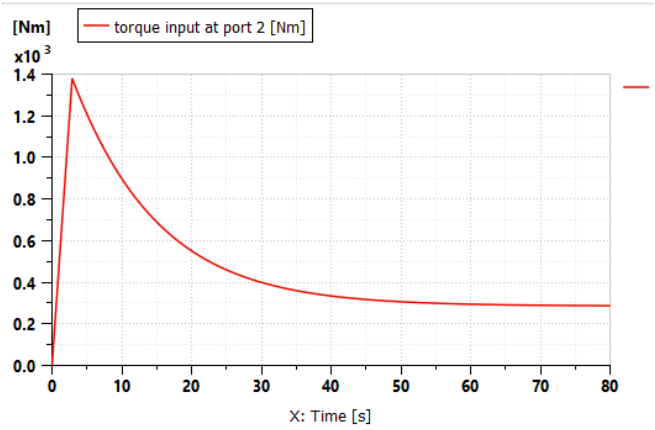


Figure 9 Simulated torque input profile at one axle of the minibus (Siemens Digital Industries Software, 2020)

A similar physical correlation is observed for the heavier minibus platform. At the initial launch point, the single axle torque sharpens dramatically to a peak of approximately 1480 Nm. This higher starting effort is directly dictated by the increased structural inertia of the vehicle operating under realistic prime mover limitations. Following the successful disengagement of the SAHR brakes, the torque profile exhibits a gradual exponential decay as the minibus accumulates momentum, maintaining a steady energy transfer throughout the extended transient regime. By the 55th second, the torque asymptotically levels off at a quasi-steady value of approximately 290 Nm.

Next, diagrams of resistive load of the vehicles are shown in Figures 10 and 11.

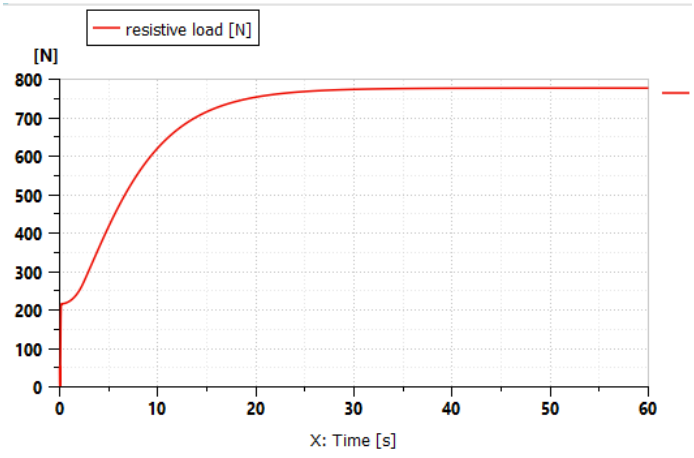


Figure 10 Simulated resistive load of the mini-truck (Siemens Digital Industries Software, 2020)

For the lightweight mini-truck, the resistive load initiates at approximately 214 N during the standstill phase—reflecting the combined baseline of rolling resistance and static headwind drag—before escalating quadratically to an

asymptotic cruising threshold of roughly 775 N. In contrast, the heavier minibus platform exhibits a significantly higher baseline resistance of approximately 500 N due to its 3500 kg chassis, progressively scaling up over an extended transient regime to stabilize at a quasi-steady value of 1732 N. For both vehicle configurations, the non-linear, parabolic progression of the curves accurately validates the quadratic influence of aerodynamic drag as velocity increases, confirming that a precise mechanical and fluid-power equilibrium is established once the maximum cruising limits are reached.

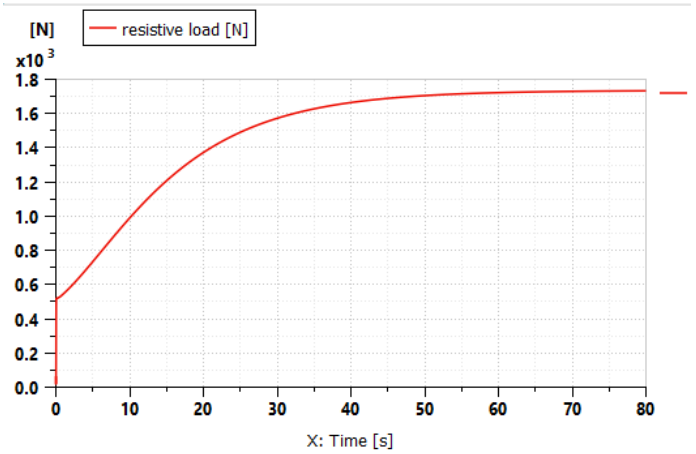


Figure 11 Simulated resistive load of the minibus (Siemens Digital Industries Software, 2020)

The total mechanical power demand delivered by the prime mover are shown in Figures 12 and 13.

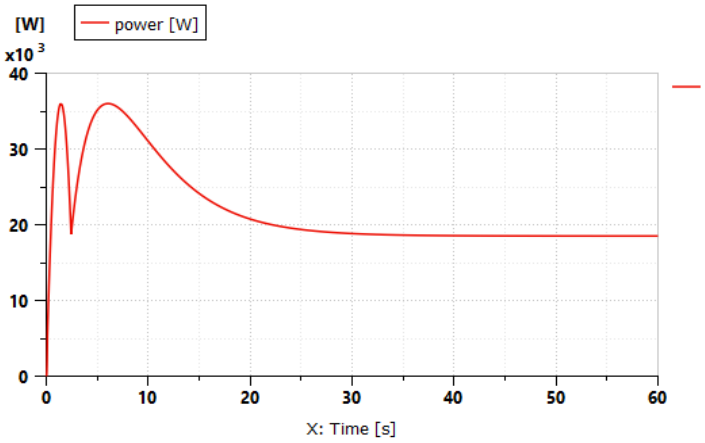


Figure 12 Simulated engine power of the mini-truck (Siemens Digital Industries Software, 2020)

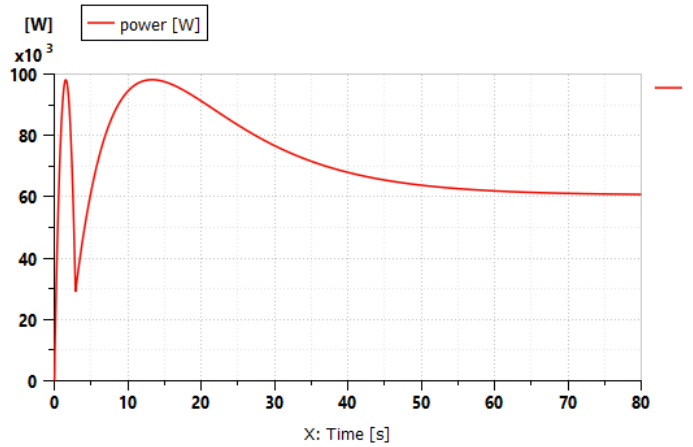


Figure 13 Simulated engine power of the minibus (Siemens Digital Industries Software, 2020)

Both profiles exhibit a highly realistic dual-peak transient behavior directly linked to the operational milestones. The initial sharp peak—reaching approximately 36 kW for the light utility truck and 95 kW for the heavier minibus—corresponds to the intensive energy throughput required to build pilot pressure within the closed hydraulic loops and successfully disengage the SAHR hub brakes. Immediately following this launch phase, a temporary drop occurs as static vehicle inertia is overcome, which is then followed by a secondary broad peak (36 kW and 98 kW, respectively) representing the maximum energy allocation during dynamic acceleration. Beyond the transient regimes, as both platforms establish aerodynamic and mechanical equilibrium, the mechanical power demand asymptotically

stabilizes at constant quasi-steady state values of approximately 18.5 kW for the mini-truck and 61 kW for the minibus.

The effective mechanical power delivered to the vehicle's driving axle is illustrated in Figures 14 and 15.

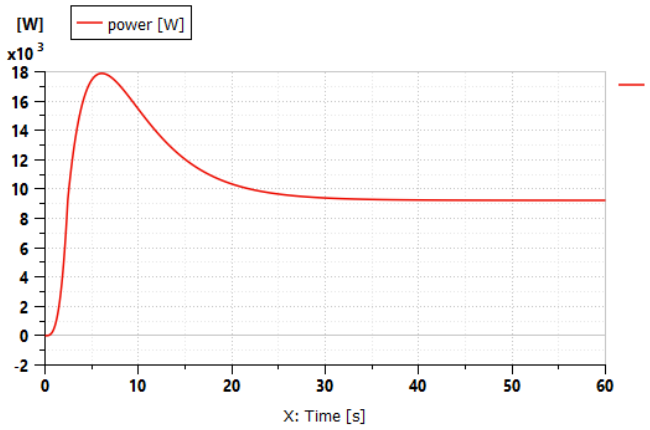


Figure 14 Simulated axle power of the mini-truck (Siemens Digital Industries Software, 2020)

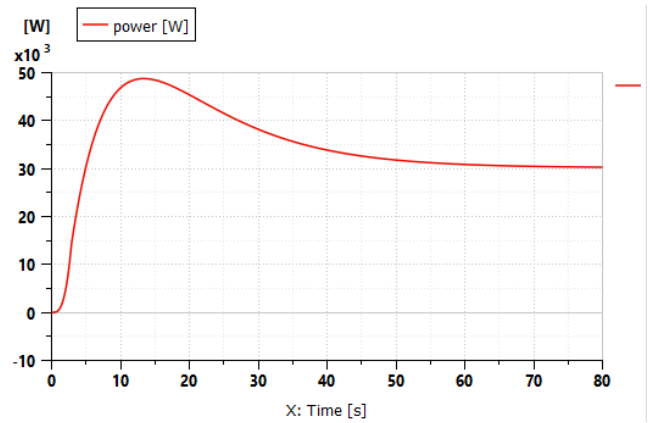


Figure 15 Simulated axle power of the minibus (Siemens Digital Industries Software, 2020)

During the initial standstill interval (0–2 s), the axle power remains at zero for both configurations until the SAHR brakes are fully disengaged. Throughout the intensive acceleration phase, the mini-truck axle power surges to a peak of approximately 18 kW, while the heavier minibus reaches a maximum axle power of 48 kW to overcome its structural inertia. In the steady-state cruising regime, the axle power asymptotically stabilizes at roughly 9.2 kW for the light truck and 30 kW for the minibus. Comparing these traction outputs to the total engine power profiles (Figures 13 and 14) clearly quantifies the dynamic volumetric and mechanical losses within the hydrostatic circuit, providing the required numerical verification for the overall drivetrain efficiency under continuous loading.

To assess operational limitations under severe conditions, a separate simulation evaluates vehicle traction on a steep 4,5° road gradient (8% gradient) (AASHTO, 2018). To ensure a rigorous comparison, all hardware and fluid parameters remain identical to those in Tables 1 and 2. This analysis focuses on how continuous gravity loading alters the drivetrain kinematics, pressure profiles, and volumetric leakage. The results are shown in Figures 16 – 25.

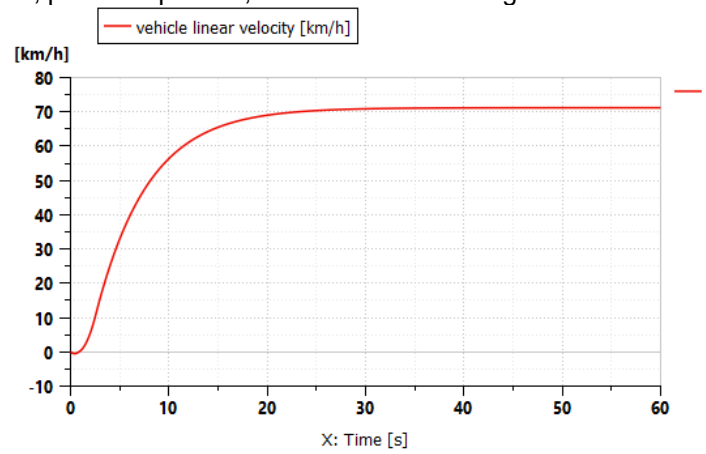


Figure 16 Diagram of simulated mini-truck velocity under the slope of 8% (Siemens Digital Industries Software, 2020)

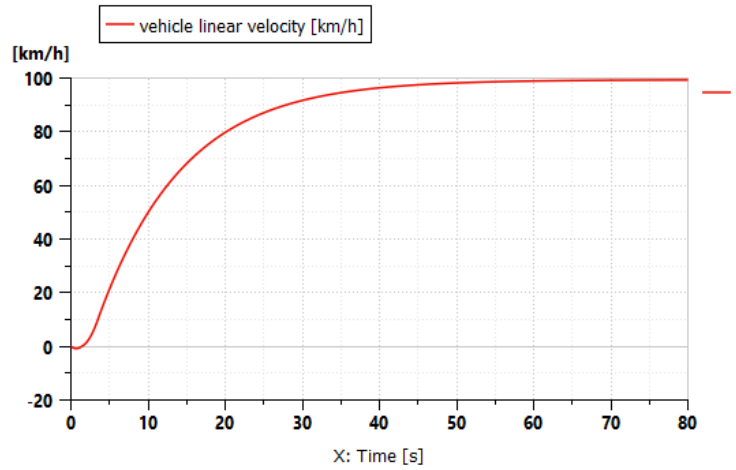


Figure 17 Diagram of simulated minibus velocity under the slope of 8% (Siemens Digital Industries Software, 2020)

Compared to the level road simulations, the introduction of a constant 8% road gradient causes a noticeable drop in the maximum cruising velocities for both platforms due to the continuous gravitational loading. Specifically, the maximum stabilized speed decreases from 85 km/h to approximately 71 km/h for the mini-truck, and from 125 km/h to roughly 97 km/h for the minibus, validating the realistic power limitations of the configured prime mover under steep incline profiles.

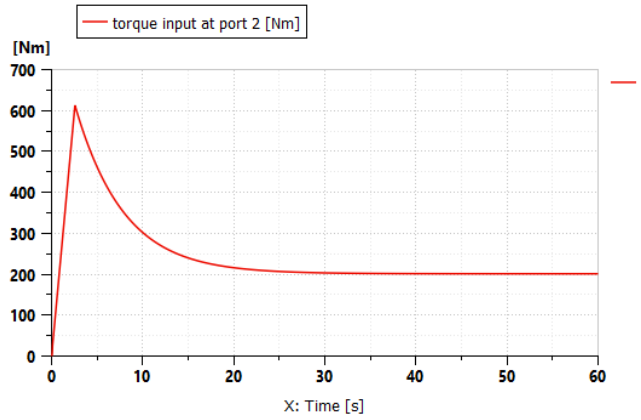


Figure 18 Diagram of simulated mini-truck axle torque under the slope of 8% (Siemens Digital Industries Software, 2020)

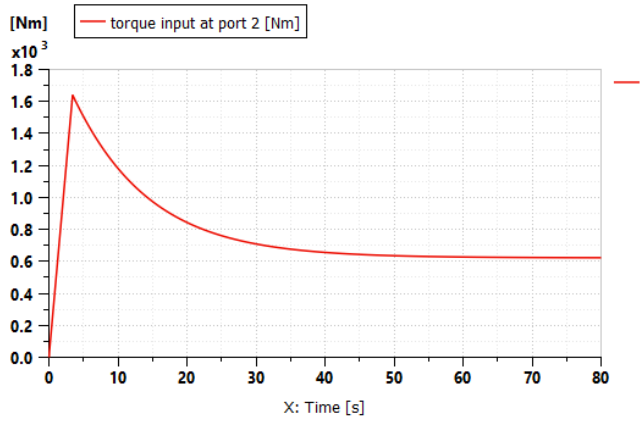


Figure 19 Diagram of simulated minibus axle torque under the slope of 8% (Siemens Digital Industries Software, 2020)

Overcoming the continuous gravity component on the 8% incline forces a substantial upward shift in torque baselines, with the mini-truck requiring a steady-state value of 200 Nm compared to its original 105 Nm level-road baseline. Similarly, the heavier passenger platform demands a much higher continuous cruising effort of approximately 620 Nm, while its launching peak sharpens to 1630 Nm, clearly capturing the severe load conditions now acting on the hydrostatic drive.

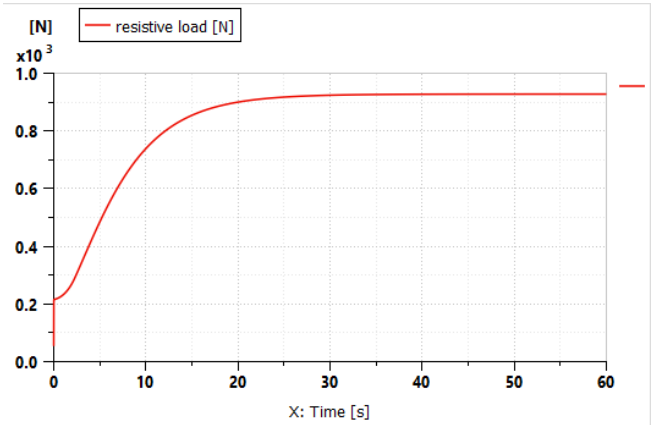


Figure 20 Simulated mini-truck resistive load under the slope of 8% (Siemens Digital Industries Software, 2020)

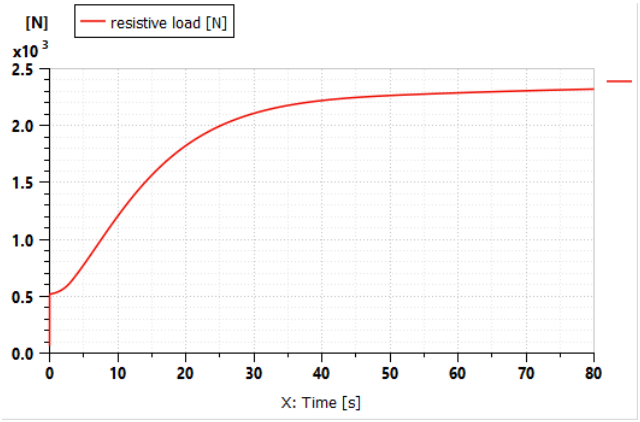


Figure 21 Simulated minibus resistive load under the slope of 8% (Siemens Digital Industries Software, 2020)

A significant amplification in the continuous load profiles is observed as the vehicles transition to the uphill simulation scenario. Cruising at maximum stabilized speeds requires a sustained tractive effort of approximately 930 N for the light utility truck, whereas the heavier passenger platform levels off at a demanding 2300 N. This smooth parabolic growth from the initial static thresholds accurately maps the combined impact of rolling friction, aerodynamic forces, and constant gravity, confirming that the hydrostatic system successfully maintains equilibrium under severe duty conditions.

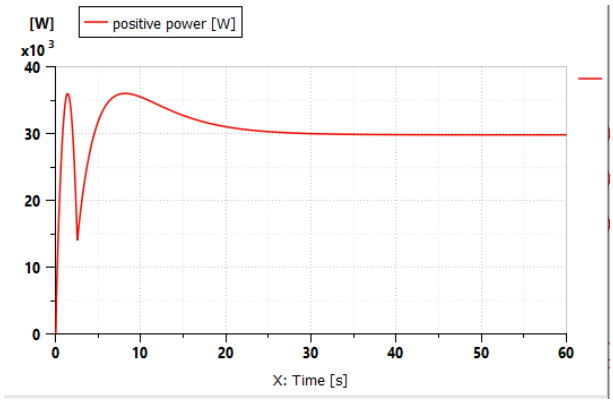


Figure 22 Simulated mini-truck engine power under the slope of 8% (Siemens Digital Industries Software, 2020)

The mechanical power demanded from the prime mover escalates significantly to overcome the combined gravitational and aerodynamic loads during the uphill transit. Both platforms retain the characteristic dual-peak transient distribution, where the initial torque surge for brake disengagement forces a sharp power draw of 36 kW for the light truck and 97 kW for the minibus. Following a brief drop as the static resistance is broken, dynamic acceleration drives a secondary energy peak before the power profiles asymptotically level off at their respective cruise baselines. Due to the constant incline gravity, the final steady-state power requirement locks at 30 kW for the utility vehicle and 94 kW for the passenger platform, successfully demonstrating a rigorous and closed energy balance within the limited boundaries of the HPU submodel.

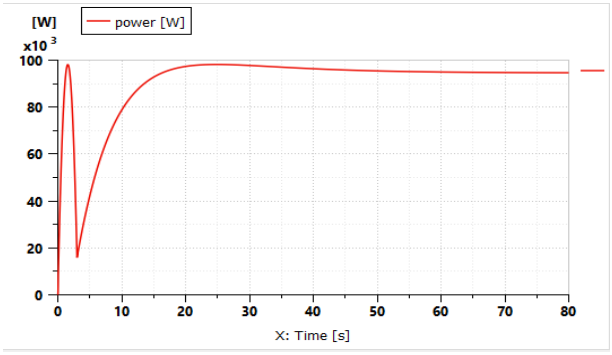


Figure 23 Simulated mini-truck engine power under the slope of 8% (Siemens Digital Industries Software, 2020)

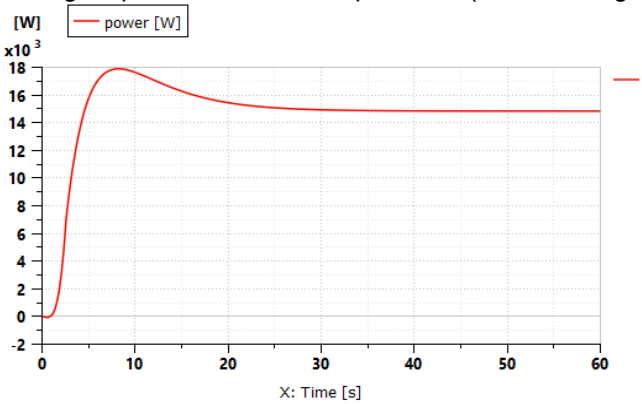


Figure 24 Simulated mini-truck axle power under the slope of 8% (Siemens Digital Industries Software, 2020)

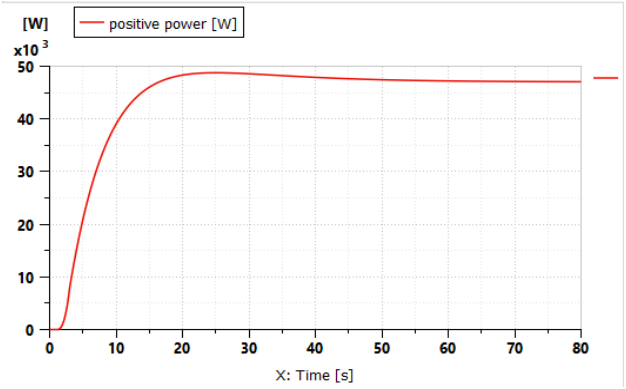


Figure 25 Simulated minibus axle power under the slope of 8% (Siemens Digital Industries Software, 2020)

The mini-truck axle power levels off at approximately 15 kW after overcoming a transient acceleration peak of 18 kW. Conversely, the more massive passenger platform requires a far higher continuous traction output of roughly 47 kW, stabilizing smoothly after a transient peak of 48.5 kW. These elevated thresholds represent a substantial increase from the respective level-road baselines of 9.2 kW and 30 kW, directly quantifying the additional tractive power required to counteract gravitational resistance.

Overall, the obtained simulation results demonstrate that the proposed hydrostatic drivetrain is capable of providing the required vehicle motion under both level-road and inclined-road operating conditions. The developed multi-domain models provide a suitable basis for evaluating the dynamic behaviour of the investigated configurations and for further optimization of the main hydrostatic drivetrain parameters.

CONCLUSIONS

In this work, a vehicle propulsion system concept based on the application of a multi-stroke radial piston hydraulic motor as an alternative solution for light utility vehicles and minibuses was successfully analysed and numerically evaluated. Through the development of a mathematical and multi-domain simulation model in the Simcenter Amesim environment, the power transmission characteristics, torque generation, and dynamic response of the vehicle under representative operating conditions were investigated, including the effects of headwind and road gradient.

The updated simulation results confirm the physical feasibility of the proposed hydrostatic propulsion system under realistic prime mover power limitations. For the light utility truck, the system achieved a maximum steady-state velocity of 85 km/h on a level road, with an individual wheel starting torque peak of approximately 580 Nm. For the heavier minibus platform, configured with an optimized pump displacement of 500 cm³/rev, the system achieved a steady-state velocity of 125 km/h on level terrain and developed a peak single-hub launch torque of approximately 1480 Nm, demonstrating the high-torque low-speed (HTLS) characteristics of the proposed drive. Furthermore, simulations under an 8% road gradient demonstrated the expected performance reduction caused by continuous gravitational loading, with steady-state velocities decreasing to approximately 71 km/h for the light utility truck and 97 km/h for the minibus, respectively. The calculated overall powertrain efficiency stabilized at approximately 49–50% during steady-state cruising for both vehicle configurations, representing the ratio between the mechanical power delivered to the driving axles and the hydraulic power supplied to the powertrain.

Compared with conventional mechanical drivetrains, which generally provide higher transmission efficiencies at high vehicle speeds but require stepped gearboxes, cardan shafts, differentials, and associated mechanical components, the proposed decentralized hydrostatic concept eliminates the need for these elements at the wheel ends. This architecture provides greater freedom for packaging, including potential low-floor integration in minibuses, while enabling continuously variable transmission characteristics without discrete gear shifts. Compared with battery electric vehicle (BEV) architectures, which generally provide higher drivetrain energy efficiency, the proposed hydrostatic system offers high torque density and favourable torque-to-weight characteristics, making it particularly attractive for heavy-duty and low-speed utility applications where compact and continuously controllable high-torque propulsion is required.

Future research will focus on further optimization of volumetric efficiency and leakage-related parameters, investigation of the thermal behaviour of the hydraulic fluid under prolonged loading, and experimental validation of the developed simulation model on a physical vehicle prototype.

REFERENCES

Abaitancei, H., Radu, S., Muntean, B., Irmia, C. (2016). Multi-domain and durability analysis of a hybrid hydraulic vehicle, *Applied Mechanics and Materials*, 823, 217-222. https://doi.org/10.4028/www.scientific.net/AMM.823.217

American Association of State Highway and Transportation Officials (AASHTO), 2018. *A Policy on Geometric Design of Highways and Streets* (7th ed.). AASHTO, Washington, DC.

Auto-Data. (n.d.). Vehicle technical specifications. Retrieved from auto-data.net

Bašta, T. M. (1986). *Mechanical hydraulics*, Faculty of mechanics, Belgrade.

Carfolio. (n.d.). *Automobile specifications and characteristics*. Retrieved from carfolio.com

Dindorf, R. (2024). Functional safety of the hydraulic drive control system of a tracked undercarriage. *The Archives of Automotive Engineering - Archiwum Motoryzacji*, 103(1), 21-37. https://doi.org/10.14669/AM/178310

Giavarini, F. (2022). *Analysis and Simulation of a Radial Piston Hydraulic Motor* [Master's thesis, Politecnico di Torino]

Guzzella, L. & Sciarretta, A. (2005). *Vehicle propulsion systems: Introduction to modeling and optimization* (2. ed.). ETH Zurich. https://doi.org/10.1007/3-540-28853-8

Krstić, B. (2003). *Hidrodinamički prenosnici snage u agregatima motornih vozila* [Hydrodynamic power transmitters in motor vehicle units] (Monograph). Faculty of mechanics, Kragujevac.

Li, C., Jiang, T., Liu, C., Xu, H., & Shi, G. (2024). Investigation of the leakage in the flow distribution pair of radial piston hydraulic motors through CFD analysis and experiments. Flow Measurement and Instrumentation, 96 102555. https://doi.org/10.1016/j.flowmeasinst.2024.102555

Mannesmann R. (1998). *Hydrostatic transmissions for wheeled and tracked vehicles*. Technical Handbook, Rexroth Hydraulics.

Popovici, V., Grigoras, I. R., Rakosi, E., Ulian, T. M., Manolache, G., Popa, A. G., & Petrovan, S. (2026). A new approach to in-wheel motor solutions for electric vehicles. *World Electric Vehicle Journal*, 17(2), 87. https://doi.org/10.3390/wevj17020087

Savić, V. (1986). *Oil hydraulics, hydraulic components and systems*, Zenica.

Simcenter Amesim, Siemens Digital Industries Software, 2020.

Sonale balu. (2024). *Understanding how a tracked vehicle works*.

Tanaka, K., Okazaki, T., & Urabe, T. (2013, 6-9 October). Comparative study on dynamic characteristics of hydraulic, pneumatic and electric motors. *Proceedings of the ASME/BATH 2013 Symposium on Fluid Power and Motion Control. ASME/BATH 2013 Symposium on Fluid Power and Motion Control.* Sarasota, Florida, USA. https://doi.org/10.1115/FPMC2013-4459

Totten, G. E., & De Negri, V. J. (Eds.). (2012). Handbook of Hydraulic Fluid Technology (2nd ed.). CRC Press.

Wong, J. Y. (2008). *Theory of ground vehicles* (4th ed.). John Wiley & Sons.

World Meteorological Organization. (2021). *Manual on Codes (The Beaufort Wind Scale)*. Geneva, Switzerland: WMO.